Author/s:
Krishnamurthi, V;Khan, H;Ahmed, T;Zavabeti, A;Tawfik, SA;Jain, SK;Spencer, MJS;Balendhran, S;Crozier, KB;Li, Z;Fu, L;Mohiuddin, M;Low, MX;Shabbir, B;Boes, A;Mitchell, A;McConville, CF;Li, Y;Kalantar-Zadeh, K;Mahmood, N;Walia, S

Title:
Liquid-Metal Synthesized Ultrathin SnS Layers for High-Performance Broadband Photodetectors

Date:
2020-11-12

Citation:
Krishnamurthi, V., Khan, H., Ahmed, T., Zavabeti, A., Tawfik, S. A., Jain, S. K., Spencer, M. J. S., Balendhran, S., Crozier, K. B., Li, Z., Fu, L., Mohiuddin, M., Low, M. X., Shabbir, B., Boes, A., Mitchell, A., McConville, C. F., Li, Y., Kalantar-Zadeh, K. ,... Walia, S. (2020). Liquid-Metal Synthesized Ultrathin SnS Layers for High-Performance Broadband Photodetectors. Advanced Materials, 32 (45), https://doi.org/10.1002/adma.202004247.

Liquid-metal synthesised ultra-thin SnS layers for high-performance broadband photodetectors

Vaishnavi Krishnamurthi[1], Hareem Khan[1], Taimur Ahmed[1,2], Ali Zavabeti[1,3], Sherif Abdulkader Tawfik[4], Shubhendra Kumar Jain[1,2,5,6], Michelle J. S. Spencer[4], Sivacarendran Balendhran[7], Kenneth B Crozier[7,8,9], Ziyuan Li[10], Lan Fu[10], Md Mohiuddin[1], Mei Xian Low[1,2], Babar Shabbir[11], Andreas Boes[1], Arnan Mitchell[1], Christopher F McConville[4], Yongxiang Li[1], Kourosh Kalantar-Zadeh[12], Nasir Mahmood[1,]* and Sumeet Walia[1,2]**

[1]School of Engineering, RMIT University, 124 La Trobe Street, Melbourne, VIC, 3001, Australia

[2]Functional Materials and Microsystems Research Group and the Micro Nano Research Facility, RMIT University, 124 La Trobe Street, Melbourne, VIC 3001, Australia

[3]Department of Chemical Engineering, The University of Melbourne, VIC 3010, Australia

[4]School of Science, RMIT University, Melbourne, VIC 3001, Australia

[5]Sensor Device Metrology Group, CSIR - National Physical Laboratory (CSIR-NPL), Dr K. S. Krishnan Road, New Delhi-110012, India.

[6]Academy of Scientific & Innovative Research, (AcSIR), CSIR-HRDC Campus, Ghaziabad, Uttar Pradesh 201002, India.

[7]School of Physics, The University of Melbourne, 3010, Australia.

[8]Department of Electrical and Electronic Engineering, The University of Melbourne, VIC 3010, Australia

[9]Australian Research Council (ARC) Centre of Excellence for Transformative Meta-Optical Systems, The University of Melbourne, VIC 3010, Australia

[10]Australian Research Council (ARC) Centre of Excellence for Transformative Meta-Optical Systems, The Australian National University, Canberra, ACT 3001, Australia

[11]Department of Materials Science and Engineering, Monash University, Clayton, Victoria, 3800, Australia

This is the author manuscript accepted for publication and has undergone full peer review but has not been through the copyediting, typesetting, pagination and proofreading process, which may lead to differences between this version and the Version of Record. Please cite this article as doi: 10.1002/adma.202004247.

[12]School of Chemical Engineering, University of New South Wales (UNSW), Sydney, NSW 2052, Australia

*Correspondence to:, nasir.mahmood@rmit.edu.au, taimur.ahmed@rmit.edu.au, sumeet.walia@rmit.edu.au

ABSTRACT

Atomically thin materials face an ongoing challenge of scalability, hampering practical deployment despite their fascinating properties. Tin monosulfide (SnS), a low-cost, naturally abundant layered material with a tunable bandgap, displays properties of superior carrier mobility and large absorption coefficient at atomic thicknesses, making it attractive for electronics and optoelectronics. However, lack of successful synthesis techniques to prepare large area and stoichiometric atomically-thin SnS layers (mainly due to the strong interlayer interactions) has prevented exploration of these properties for versatile applications. Here, we print SnS layers with thicknesses varying from a single unit cell (0.8 nm) to multiple stacked unit cells (~1.8 nm) synthesised from metallic liquid tin, with lateral dimensions on the millimetre scale. We reveal that these large area SnS layers exhibit a broadband spectral response ranging from deep ultraviolet (UV) to near infrared (NIR) wavelengths (*i.e.*, 280 nm to 850 nm) with fast photodetection capabilities. For a single unit-cell thick layered SnS, our photodetectors show upto three orders of magnitude higher responsivity (927 A W^{-1}) than commercial photodetectors at a room-temperature operating wavelength of 660 nm. This study opens a new pathway to synthesise reproduceable nanosheets of large lateral sizes for broadband, high-performance photodetectors. It also provides important technological implications for scalable applications in integrated optoelectronic circuits, sensing and biomedical imaging.

INTRODUCTION

Two-dimensional (2D) materials have been a major focus for a plethora of scientific discoveries, ever since the isolation of graphene from its bulk crystal. However, the tremendous potential of post transition metal monochalcogenides (*1-3*) such as the Group IV monochalcogenides (*MX*, *M* = Sn, Ge, Pb, *etc* and *X* = S, Se) remains relatively untapped (*4*). Theoretical studies of these materials have revealed peculiar electronic and optoelectronic properties at their quantum limit but are yet to receive an experimental thrust (*5*) primarily due to the inability to obtain large aspect ratios. Semiconducting SnS is a representative member of the family of post transition metal monochalcogenides that exist in an orthorhombic layered structure (*6, 7*).The buckled structure of SnS is held together with weak van der Waals (vdW) forces between the layers exhibiting structural anisotropy, a feature very similar to the isoelectronic structure of black phosphorus (BP) (*1, 7*) (See **Note 1**, Supporting Information). As a *p*-type semiconductor, SnS has both indirect and direct bandgap energies reported in the range ~1.0 – 1.3 eV and ~1.3 – 1.5 eV, respectively (*7*). The bandgap tunability allows it to exhibit a combination of desirable electronic and optoelectronic properties (*8-10*) that include large absorption coefficient (*11*) across a wide wavelength range, tunable electrical conductivity (*12*) and high carrier mobility (*6*). This renders SnS a suitable candidate for multidisciplinary applications such as photodetectors (*13*), photovoltaic cells (*14*), field-effect transistors (*15*) and spin-valley lasers (*16*). However, conventional growth and synthesis strategies such as chemical vapour deposition (CVD) and physical vapour deposition (PVD) have failed to attain good quality atomically-thin SnS due to the formation of uncontrolled grain orientations, defects and impurities (*17-19*). Strong inter layer interactions resulting from lone pair electrons associated with each S–atom is a prominent reason for the inability to isolate ultra-thin layers of SnS (*6*) using established mechanical cleaving processes. These interactions are stronger than the vdW forces exhibited between Sn–S layers (*20*), that generate substantial energy distribution and strong charge transfer resulting in electronic coupling between adjacent layers (*20, 21*). Low temperature liquid metals present an opportunity to obtain ultrathin layers (*22, 23*) with relatively large lateral dimensions. As a material that can be processed at low temperature, SnS is an excellent candidate to be synthesised in its atomically thin-form using this approach and be deployed as functional layers for wide-band photodetectors that have not been reported to date.

Here, we deploy a unique synthesis technique that results in a single unit cell thick SnS layers with lateral dimensions up to the millimetre scale. The technique relies on sulfurising the top surface of molten tin (Sn). Subsequently, we isolate Sn–S that appears at the top surface of the molten Sn using a vdW transfer technique (**Figure 1a** and **Note 2**, Supporting Information) (*22, 24*). The non-polarised nature of the molten Sn results in the absence of macroscopic forces between Sn and its sulfurised skin, allowing a clean delamination. As such, the as-obtained large-area SnS layers are utilised to demonstrate ultra-sensitive broadband photodetectors with more than three orders of magnitude higher responsivity (10^2–10^3 A W^{-1}) than commercial photodetectors and detectivity in the range (10^9–10^{10} Jones) for wavelengths ranging from 280 nm to 850 nm. Considering the quest for miniaturising devices, this work showcases a high-performance SnS photodetector with a functional layer that is sub-1 nm thick. This provides an exciting pathway towards miniaturising light detection devices which will expand their breadth of applications.

RESULTS

As a substrate, we used doped silicon with a 300-nm thick layer of SiO_2. The as-grown SnS layers, on the surface of liquid metal Sn, were transferred onto a pre-cleaned substrate through vdW transfer technique. In **Figure 1b** and **Note 3**, Supporting Information, optical microscopy images clearly show a large lateral synthesis of SnS layers. The low magnification transmission electron microscopy (TEM) image reveals the growth of homogenous SnS layers with ultrathin features (**Figure 1c**). The selected area electron diffraction (SAED) pattern further reveals single crystalline features of synthesized SnS layers and their perfect orthorhombic crystal structure (**inset** of **Figure 1c**). Confirmation of single crystallinity was obtained by acquiring SAED measurements across different locations of the SnS layer (**Note 4**, Supporting Information). The lattice spacing of 2.8 Å correspond to the (040) plane according to the PDF#39-0354 dataset. The high-resolution TEM (HR-TEM) images show the unidirectional crystalline layers with an inter-planar distance of 2.8 Å which also corresponds to the (040) plane (**Figure 1d**). **Figure 1e** shows a representative atomic force microscopy (AFM) topological scan of as-synthesized single unit cell thick SnS layers. Here, single unit cell thick SnS layers imply two layers of SnS stacked one on top of the other and reveal a thickness of 0.8 nm (**Figure 1f**). The representative AFM scan of two-unit cell

(that we refer to as multiple unit cell) thick layered SnS shows a thickness of ~1.8 nm (**Note 5**, Supporting Information).

To further confirm the growth of monochalcogenide SnS layers, Raman spectroscopy was performed which shows active vibrational modes at 94.21 cm^{-1},185.61 cm^{-1} and 219.6 cm^{-1} that can be assigned to the A_g phonon modes and the peak at 158.21 cm^{-1} assigned to B_{3g} orthorhombic mode of layered SnS (**Figure 1g**) (*20, 25*). The Raman spectra obtained from the layers before and after device fabrication were identical and did not show any discernible change. The Raman peaks only show the vibrational modes associated with SnS (*18, 26*). Vibrational modes that can be associated with other stoichiometries and oxides are absent indicating the presence of SnS. Other characteristics such as the optical absorbance and bandgap are also in alignment with expected values for SnS (*27*). EDS was performed to additionally assess the Sn and S ratios which was ~ 1:1 (see **Note 6**, Supporting Information). A slightly lower ratio of S than Sn which can be expected due to the interaction of atomically thin SnS with high energy X-rays.

Chemical states and stoichiometry of the synthesized SnS sample was investigated by X-ray photoelectron spectroscopy (XPS) measurements. Sn 3d and S 2p core level spectra were recorded and de-convoluted into their corresponding chemical species as shown in **Figures 1h** and **1i**, respectively. The Sn 3d core level spectrum reveals a spin orbit splitting of 8.4 eV which corresponds to the Sn $3d_{3/2}$ and Sn $3d_{5/2}$ spin states. The Sn 3d core level spectrum is de-convoluted and fitted with only one contribution representing Sn–S chemical state. The peak position at 486.1 eV and 494.5 eV corresponds to the Sn $3d_{5/2}$ and Sn $3d_{3/2}$ spin states for Sn–S. The S 2p core level spectra were also recorded to verify it as shown in **Figure 1i**. The S 2p core level spectrum reveals a spin orbit splitting of 1.1 eV which corresponds to S $2p_{3/2}$ and S $2p_{1/2}$ spin states. The de-convoluted S 2p spectrum also exhibits only one chemical interaction for S 2p where peak positions at 161.7 eV and 162.8 eV are associated to the S $2p_{3/2}$ and S $2p_{1/2}$ of S–Sn chemical interaction. This confirms the formation of only Sn–S in the synthesized sample. The de-convoluted XPS data of SnS sample is well supported with the previous literature (*17, 28, 29*).

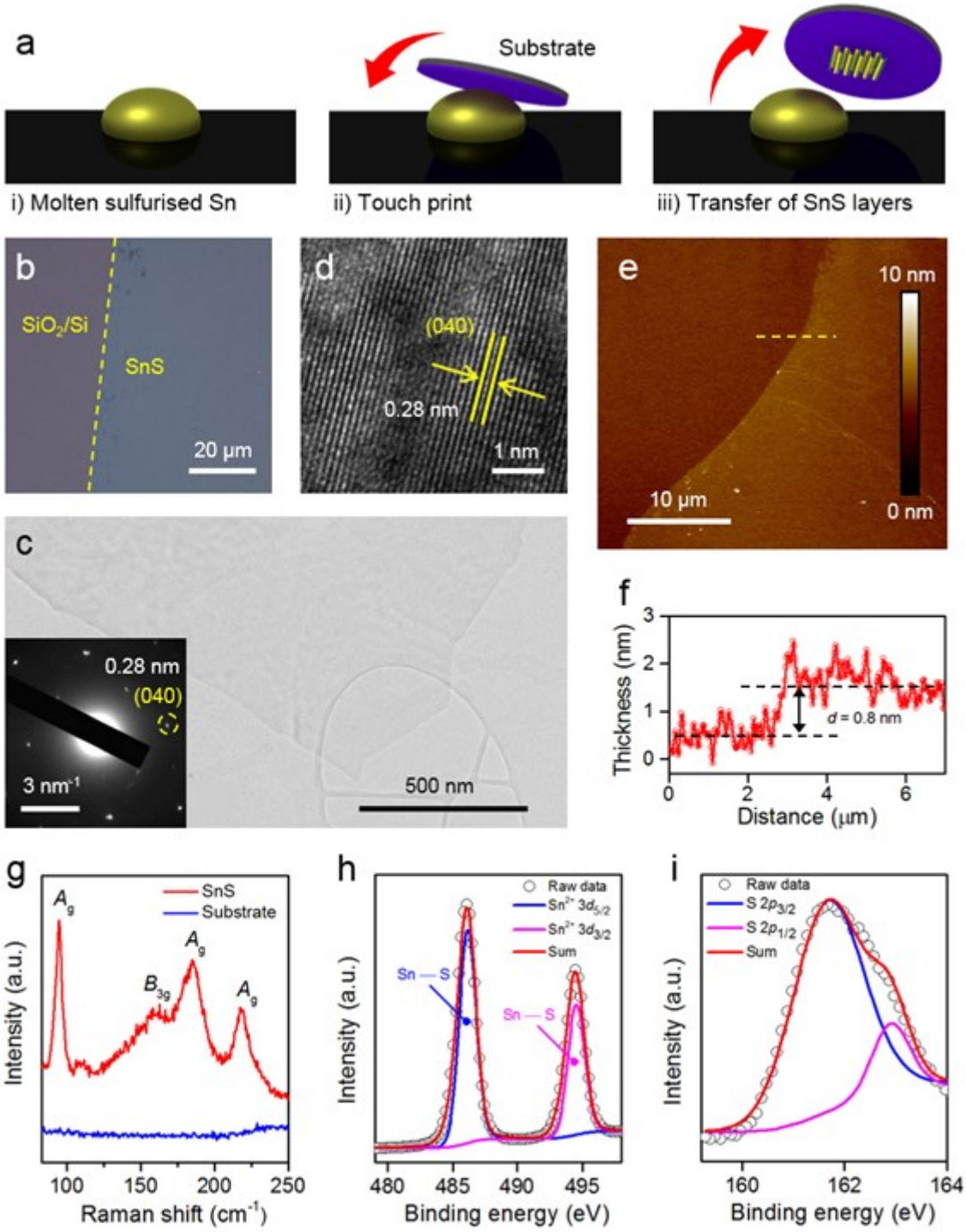

Figure 1 | SnS synthesis schematic and characterisations (a) Schematic representation of the synthesis process. Elemental tin synthesised inside the glove box is melted on a reference substrate using a heater. The surface of the metal quickly forms a sulfide layer due to its interaction in a hydrogen sulfide (H_2S) environment. When a cleaned substrate is brought in contact with the molten metal, the van der Waals force between tin sulfide and the SiO_2 surface provides adhesion of the material onto the substrate. Delamination of the sheet becomes possible due to a weak macroscopic force that exists between the parent metal and the metal sulfide layer. (b) Optical microscope image of single unit cell thick SnS serving as the conductive channel in our

photodetector. (c) TEM image of SnS synthesized in a sulfide environment, using a TEM grid as the substrate. Inset of (c), SAED image of the sample indexed to SnS (d) HRTEM image of the sample display a d-spacing of 2.8 Å matched to (040) plane. (e) AFM image of the delaminated single unit cell thick SnS layers (f) Thickness profile of the AFM image reveal a thickness of 0.8 nm. (Thickness for the AFM = 0.3×2 nm - two layers + vdW gap of 0.2 nm). (g) Raman spectrum of layered SnS measured under ambient conditions along with the spectrum of the SiO_2/Si substrate (h) XPS spectra of Sn–S $3d_{5/2}$ and $3d_{3/2}$ exposing peaks at 486.1 eV and 494.5 eV. (i) XPS spectra of the $S2p_{3/2}$ and $S2p_{1/2}$ peaks at 161.7 eV and 162.8 eV.

The electronic band structure of monolayer, bilayer and trilayer SnS were obtained using density functional theory (DFT) calculations (see **Note 7**, Supporting Information). In the context of this study, we intend to gain insights into photocurrent generation in SnS. The band structures, band transitions and associated band gap values of the monolayer, bilayer and trilayer SnS structures are depicted in **Figures 2a-c**. We also experimentally measured band gap values (**Figure 2d, e**). The indirect bandgap (E_i) values derived *via* Tauc plot from absorbance measurements reveal a value of 1.81 eV for a single unit cell thick layers and 1.41 eV for multiple unit cell thick (2 single unit cell thick) SnS layers as shown in **Figure 2d** and **Figure 2e**, respectively. These values closely correlate with the values obtained *via* the DFT calculations. Simplified band structures shown in the insets of **Figures 2d** and **Figure 2e** have been attained using photoelectron spectroscopy in air (PESA) and XPS valence band measurements. Obtained Fermi level values of -4.75 eV from PESA measurement and valence band value of -0.58 eV from XPS valence analysis indicate the material is *p*-type in nature (*30*) (see **Note 8**, Supporting Information). The hole mobility (~35 $cm^2 V^{-1} s^{-1}$) and p-type nature of SnS is also confirmed using Hall-effect mobility measurement and by obtaining the transfer characteristics in a back-gated configuration (see **Note 9,** Supporting Information). Interestingly, **Figure 2e** reveals the presence of strong density of states (DOS) between 1.2 eV and 1.4 eV. These DOS that tend to exist within the energy bandgap of the SnS semiconductor can be associated with sulfur and/or tin vacancies in the material (*31, 32*). Such crystal defects lead to deep trap states that plays a significant role in the excitonic generation and recombination events that occur in a photodetector (*33*).

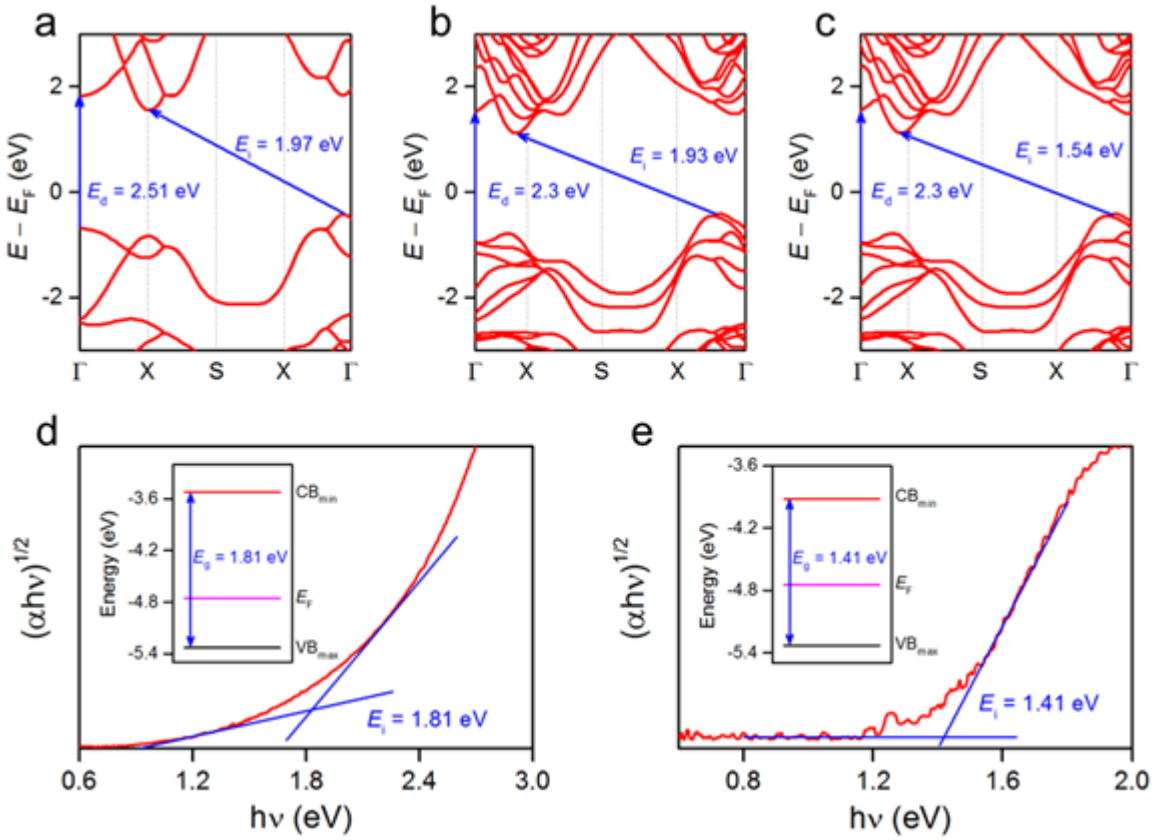

Figure 2 | DFT calculations and experimental analysis of band structure. (a) monolayer (b) bilayer (c) trilayer SnS band structures. The arrows indicate the direct (E_d) and indirect (E_i) band gap transitions and band gap values in eV. The direct band gap values (as measured at the Gamma point) are 2.51 eV for the monolayer and 2.3 eV for the bilayers and trilayers. The indirect band gap values are 1.97 eV, 1.93 eV and 1.54 eV for the mono, bi and trilayers, respectively. (d) and (e) Tauc plot estimating E_i of the material for single and multiple unit cell SnS layers. Insets of (d) and (e) show simplified electronic band diagram indicating energy gap, Fermi level, valence and conduction band edges of the layers of the associated thicknesses.

Next, we fabricate a pair of Au electrodes with a gap of 5 μm **(See Figure 3a** and **Figure S9**, **Note 10**, Supporting Information**)** on separate single and multiple unit cell thick SnS layers as the semiconducting channel. The area between the electrodes is used as the active area and included in **Table 1**. To evaluate the performance of single unit cell thick SnS layers as photodetectors, room temperature photoelectrical measurements were carried out by applying a voltage bias of 4.0 V. **Figure 3b** shows photoresponse over a broad wavelength ranging from 400 nm to 1200 nm, with maximum photocurrent obtained at a wavelength of ~620 nm. Subsequently, time-dependent photo response of the two-terminal devices was probed across a range of wavelengths spanning from UV (280 nm) to NIR (850 nm). The electrical response was acquired and repeated for 280 nm (UV B), 365 nm (UV A), 455 nm (blue), 565 nm

(green), 660 nm (red) and 850 nm (NIR) excitations respectively. Given the large area of SnS layers resulting in uniform photocurrent generation, no specific laser alignments were required.

Devices of different thicknesses (single and multiple unit cells) were probed to observe the change in photocurrent ΔI (= $I_{illumination} - I_{dark}$) at a power density of 2.5 mW/cm^2 and a voltage bias of 2.0 V. Devices with single unit cell thick SnS layers provide a maximum response at a wavelength of 660 nm. Here, the photoresponse behaviour is attributed to its band gap which limits the absorbed photons to an energy of 1.81 eV (681 nm) to generate photoexcited carriers. A relatively lower photoresponse is obtained beyond this regime, accompanied by a reduction in photocurrent in the NIR region. For multiple unit cell thick devices, the maximum response is obtained in the NIR region of the spectrum (850 nm) which is equivalent to the band gap of 1.41 eV. A linearly decreasing behaviour is observed in this case as the wavelength of incident light is sequentially reduced from 850 nm to 280 nm. To assess the repeatability of these results, photoresponse measurements were performed on more than 30 devices, for devices of both thicknesses. Photocurrents of both single unit cell and multiple unit cell thick SnS layers along with the standard deviation against each wavelength is provided in **Figures 3c** and **3d,** showing the high repeatability of results. *I-V* characteristics along with the photocurrent dynamics of single and multiple unit cell thick SnS devices is shown in **Figure S10**, **Note 10**, Supporting Information. We also simulate the optical properties of SnS to further understand the effect of SnS thickness and the substrate effects (**Figure S11, Note 11**, Supporting Information). We observe an overall increase in absorbance across the stimulated range (600 – 1200 nm) as SnS thickness increases and a further enhancement in the range (600 – 700 nm) due to the optical-cavity effect from the SiO_2/Si substrate.

The behaviour of our SnS photodetectors can be explained in terms of absorption coefficients of relatively narrow bandgap semiconductors (*14, 27*). This phenomenon is induced by a reduction in photogenerated carriers available for extraction under photon flux owing to Auger processes (*34*) and the saturation of recombination/trap states that influence the lifetime of the generated carriers (*35*). We further note that as the illumination wavelength nears the bandgap energy of SnS, the photocurrent increases. Incident photons with an energy similar to the band gaps are efficiently absorbed with lower energy loss compared to higher energy photons resulting from lower wavelength illumination (*36*). As the illumination of

devices is global, temperature differences (if any) will be similar between the two interfaces of electrodes and therefore it is safe to assume negligible contribution from the photo thermoelectric effect (*37*).

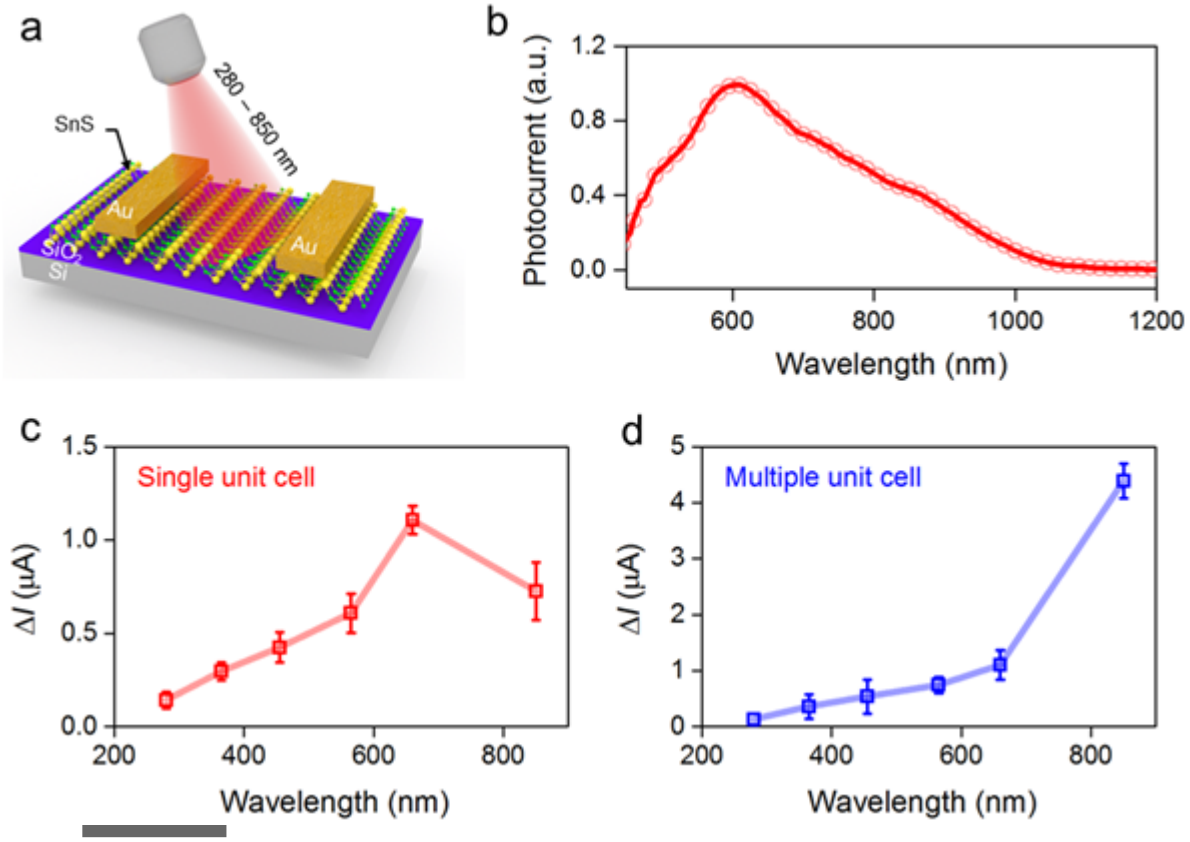

Figure 3 | Characterisation of single and multiple unit cell thick SnS layers. (a) Schematic illustration of SnS photodetector fabricated on SiO_2/Si substrate (b) Broadband photocurrent obtained at a bias of 4.0 V and power density of 1.45 nW (c) Photocurrent measured against different wavelengths for single unit cell thick SnS layers with a maximum response at 660 nm. (d) Photocurrent measured against different wavelengths for multiple-unit cell thick SnS layers with a maximum response obtained at the NIR region (850 nm) of the spectrum.

Figures 4a and **4b** shows photoresponse as a function of the incident power for devices with single and multiple unit cell thick SnS layers. The linear increase in photocurrent with increasing illumination power density can be associated with the photoconductive effect (*38*). Responsivity (*R*) is one of the most critical figures of merit used to define the performance of a photodetector. *R* of the photodetector is calculated from the formula (*39, 40*)

$$R = \frac{\Delta I}{P_{inc} \times S} \quad (1)$$

where ΔI is the change in photocurrent, P_{inc} the power density for a wavelength and S the effective area between the electrodes of the material subjected to illumination. R at an illumination intensity of 2.5 mW/cm^2 for single unit cell thick SnS device is calculated to be 927 A W^{-1} (at $\lambda = 660$ nm) and 3510 A W^{-1} for multiple unit cell thick SnS device at $\lambda = 850$ nm (**Figures 4c** and **4d**). Additionally, R for other wavelengths are in the range 10^2–10^3 A W^{-1} which indicates the ultrasensitive nature of the photodetector. We plot responsivity values for various illumination intensities (see **Figures S12a** and **S12b**, **Note 12**, Supporting Information) which reveal a decreasing trend with increasing intensities.

Noise equivalent power (NEP) is also an important parameter that governs the sensitivity of

$$NEP = \frac{i_n}{R} = \frac{(S \times \Delta f)^{1/2}}{D^*} \quad (2)$$

the photodetector and can be expressed as (*41-43*)

where i_n is the noise current and R is the responsivity of the device. The noise current of our single-unit cell and multiple unit cell thick SnS photodetector was measured with the help of a lock in amplifier (***Figure* S13**, ***Note 13***, Supporting Information). *NEP* values derived from noise current measurements were calculated to be 6.18×10^{-13} W for single unit cell-thick SnS device and 3.46×10^{-14} W for multiple unit cell thick SnS device.

Detectivity from equation (2) can be rearranged as (*41, 43, 44*),

$$D^* = \frac{(S \times \Delta f)^{1/2} \times R_i}{i_n} \quad (3)$$

where R_i is the responsivity for a wavelength, S is the effective area subjected to illumination and Δf is the bandwidth. The peak detectivity obtained at a power density of 2.5 mW/cm^2 for single unit cell thick SnS device is observed for $\lambda = 660$ nm and calculated to be 1.09×10^9 cm Hz$^{1/2}$ W^{-1} (Jones) whereas a peak detectivity of 6.83×10^{10} Jones for multiple unit cell thick SnS layers is obtained at $\lambda = 850$ nm as shown in **Figures 4e** and **4f**. Furthermore, the D^* for various power densities obtained by taking noise spectral density into

account is plotted in **Figures S12c** and **S12d**, **Note 12**, Supporting Information, explaining the photo saturation effect of the device.

The photo-conversion ability of a photodetector is defined by its external quantum efficiency

$$EQE = \frac{h \times c \times R}{e \times \lambda} \quad (5)$$

(*EQE*) expressed as (*40, 44, 45*),

where h is the Plank's constant, c is the velocity of light, e is the charge of an electron, λ is the wavelength of incident light, and R is the responsivity of the photodetector. *EQE* value obtained here for single unit cell thick SnS layers at $\lambda = 660$ nm is 1.74×10^5 % and 1.53×10^5 % for multiple unit cell thick SnS layers at $\lambda = 850$ nm when measured at an illumination intensity of 2.5 mW/cm^2, is shown in **Figures S12e** and **S12f**, **Note 12**, Supporting Information. *EQE* as a measure of voltage bias is also presented in **Figures S12g** and **S12h**, **Note 12** Supporting Information.

The response speed at various pulsed frequencies governs the operational speed of the photodetector which is crucial in determining its viability for practical applications. For instance, the ability of a photodetector to follow optical signals of various types could pave the way for its use in NIR imaging (*46*). Herein, we investigated the performance of our single unit cell and multiple unit cell thick photodetectors, for all wavelengths, which show no significant decay in the photocurrent when the frequency values varied between 0.1 Hz and 500 Hz (see **Figure S14**, **Note 14**, Supporting Information). Furthermore, the transient response times (rise and fall times) of the photocurrent was also measured for all wavelengths at a power density of 2.5 mW/cm^2. The response time is calculated by exponentially fitting the experimental data (*47*). Rise time constant (τ_r) and decay time constant (τ_d) is the time required for the photocurrent to reach 63% of its steady state value from its initial value and vice-versa (*48*). Values for τ_r and τ_d are obtained as 15.8 μs and 105 μs for single unit cell thick SnS layers, under the wavelength of 660 nm at 500 Hz illumination frequency (**Figure 4g**). Rise time (t_r) and decay time (t_d) is defined as the time required for the photocurrent to increase from 10% and reach 90% of its peak value and vice-versa (*48, 49*). The rise and fall times are calculated as $t_r = \tau_r \times 2.197$ and $t_d = \tau_d \times 2.197$, respectively (*48*). Hence, the rise and fall time obtained for single unit cell thick SnS layers at 660 nm are 34.71 μs and 230.7 μs,

respectively. Similarly, for multiple unit cell thick SnS layers, τ_r and τ_d were obtained as 22 µs and 51.5 µs under the illumination wavelength of 850 nm and illumination frequency of 500 Hz **(Figure 4h)**, which gives t_r and t_d values of 48.33 µs and 113.14 µs, respectively. It is noted that, in all cases, the rise time is faster than the decay time. A relatively slower decay time could be a result of defects present in the system, where the life time of holes is prolonged in the trapped regions of layered SnS (*49-51*).

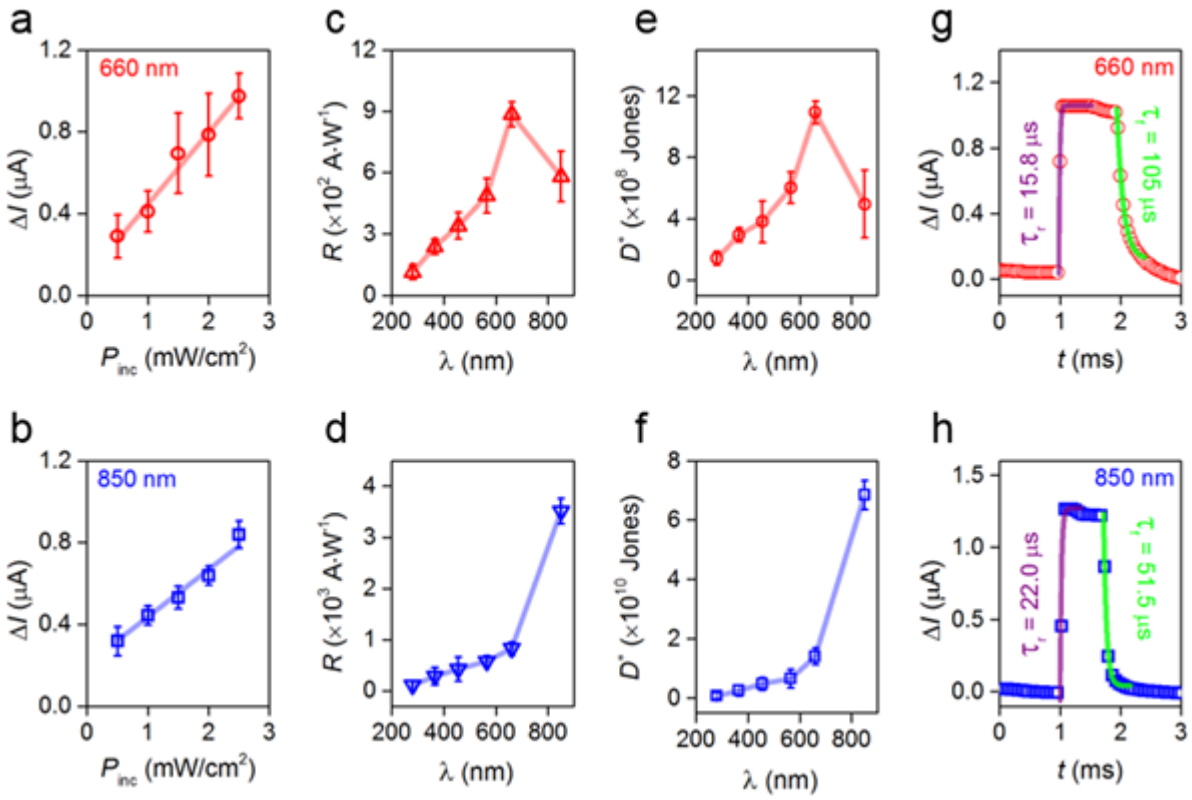

Figure 4 | Figures of merit for single unit cell thick and multiple unit cell thick SnS layers. Photocurrent at different power intensities showing a linear dependence curve for (a) single unit cell thick SnS layers under the wavelength of 660 nm and (b) multiple-unit cell thick SnS layers at 850 nm wavelength. Responsivity obtained at $P_{inc} = 2.5$ mW/cm^2 and $V_{ds} = 2.0$ V at different wavelengths for (c) single unit cell and (d) multiple unit cell thick SnS layers. Detectivity obtained at $P_{inc} = 2.5$ mW/cm^2 and $V_{ds} = 2.0$ V at different wavelengths for (e) single unit cell thick and (f) multiple-unit cell thick SnS layers. (g) Response time of single unit cell thick SnS layers at a wavelength of 660 nm at an illumination frequency of 500 Hz. (h) Response time of multiple-unit cell thick SnS layers at a wavelength of 850 nm and at a frequency of 500 Hz.

We consider the mechanism underpinning the high EQE and relatively fast response times in detail in **Note 15**, Supporting Information.

The gate dependant characteristics along with the figures of merit under different gate voltages is shown in **Note 16**, Supporting Information. Gate dependant measurements indicate that photocurrent dominates over thermionic tunnelling currents across the entire operating range of gate voltages.

Existing commercially available photodetectors are typically made from silicon (Si), gallium phosphide (GaP), germanium (Ge) and indium gallium arsenide (InGaAs). The comparison of performance parameters in **Table 1** show superior figures of merits. The responsivity and detectivity values of commercial photodetectors are in the range of 0.1 – 1 A W^{-1} and 10^{11} – 10^{13} Jones, respectively (*52*). Nevertheless, formation of large densities of defects in the growth process of materials (*53*), requirements of high processing temperature (*54*) and cryogenic cooling systems for efficient operation (*55*), incompatibility with flexible platforms and bulkiness (*53*) are some of their ongoing challenges. For instance, InGaAs based photodetectors rely on complex fabrication steps particularly requiring lattice matching and surface passivation (*56, 57*). On the other hand, SnS depicts a self-terminating lattice while being compact and showing higher responsivities in NIR range at room temperature. Also, it is to be noted that figures of merit values of commercial photodetectors mentioned in **Table 1** are recorded at a bias voltage of more than 2.0 V. So, the power consumption of the devised SnS photodetectors is relatively less in comparison to state-of-the-art photodetectors. 2D semiconductor-based photodetectors have showcased values as high as 10^{0}–10^{5} A W^{-1} for responsivity, 10^{9}–10^{16} Jones for detectivity and 10^{1} - 10^{7} % for external quantum efficiency (listed in **Table 1**). In this work, responsivities that are three orders of magnitude higher than commercial Si photodetectors (in case of Si responsivities typically drop further at longer wavelengths) and indium gallium arsenide (InGaAs) photodetectors are showcased. Taking material characteristics into consideration, Cadmium (Cd) is a heavy metal ion and extremely hazardous in nature (*58*), degradation of BP under ambient atmosphere remains a key issue till date (*59, 60*), the heavy electrons in molybdenum disulphide makes it an unfavourable material for high speed photodetection applications (*61-63*), tin disulphide (SnS_2) as another sulfide of Sn has a relatively wider band gap restricting its detection limits up to the visible range only (*64*). Sn does not suffer from such drawbacks as it is an earth abundant and relatively safe metal (*5, 65*). In addition, SnS provide high chemical stability (*5*) and air stability (*5, 65*) rendering it a truly exceptional material for leading edge applications in optoelectronics.

Materials	Wavelength	Thickness	Testing conditions	R (A/W	D^* (Jone	EQE (%)	Response time	Ref

CONCLUSIONS

In conclusion, we have successfully presented repeatable synthesis of large area single and multiple unit cell thick SnS layers by utilising vdW transfer of molten Sn onto conventional substrates. Experimental characterisations of the synthesised SnS layers confirm a reduction in band gap with increasing thickness of layers which is further validated by theoretical calculations. The alluring material properties of atomically thin layered SnS have been elucidated by demonstrating broadband photodetectors operating in 280 nm to 850 nm wavelength range. The figures of merit obtained for our broadband photodetectors show more than three order of magnitude responsivities as compared to the state-of-the-art commercial photodetectors. The stability of atomically thin SnS nanosheets even at such low thicknesses is a significant advantage. As such, our work proposes a new avenue for large area synthesis of ultra-thin layers of a representative material that cannot normally be synthesised in atomically thin form using conventional processes and adapt it for high-performance optoelectronics. This also opens pathways towards discovering the unique properties that could exist at the quantum limit of other layered materials.

				P_{inc} (mW/cm^2)	V (V)	Area (μm^2)					
2D	**SnS unit cell layers**	**660**	**~0.7**	**2.5**	**2**	**50**	**9.2×10^{2}**	**1.09×10^{9}**	**1.7×10^{5}**	**0.12**	**This work**
	SnS multiple unit cell layers	**850**	**~1.8**	**2.5**	**2**	**50**	**3.51×10^{3}**	**6.83×10^{10}**	**1.5×10^{5}**	**0.16**	**This work**
	$NiPS_3$ – nanosheet	254	4.7	0.1	10	9	1.2×10^{-1}	1.2×10^{12}	61	20.7	(*66*)
	GaSe – nanosheet	254	~4.0	1.0	5	NM	2.8	NM	1367	20	(*67*)
	CdTe – nanosheet	473	5-15	5.9	1	7	0.0006	1.0×10^{9}	NM	33.1	(*50*)
	MoS_2 – flakes	633	10-60	50.0	1	NM	0.05-0.12	10^{10}-10^{11}	NM	NM	(*68*)
	ReS_2 – flakes	532	~4.0	6.0×10^{-9}	4	2.2	8.8×10^{4}	1.2×10^{12}	2×10^{7}	$>1.0\times10^{3}$	(*69*)
	MoS_2 – flakes	561	~0.6	0.024	8	NM	8.8×10^{2}	NM	NM	1.3×10^{4}	(*61*)
	$SnSe_2$ – flakes	530	~1.5	6.4	3	NM	1.1×10^{3}	1.0×10^{10}	2.6×10^{5}	22.6	(*70*)
	Se:BP – flakes	635	10-20	61.3	0.1	5-60	15.3	NM	2993	450	(*71*)
	BP – flakes	280	18.0	0.5	0.2	NM	3.6×10^{5}	2.3×10^{13}	1.6×10^{6}	$>1.0\times10^{3}$	(*39*)
	SnS_2 – flakes	532	1-1.6	1.0×10^{-4}	NM	NM	100	NM	NM	$>1.0\times10^{4}$	(*49*)
1D	WS_2 – crystals	532	2	2.5×10^{7}	5	NM	2.5	9.9×10^{10}	583	NM	(*72*)
	CdS – nanobelt	490	200	3.0	1	NM	7.3×10^{4}	NM	1.9×10^{7}	~0.02	(*73*)

	s										
	SnS – nanobelts	800	32	2.5	1	4.5	3.0×10^{2}	6×10^{9}	4.6×10^{4}	43	(*74*)
	CdS – nanowires	375	NM	0.01	1	3.21	2.6×10^{5}	2.3×10^{16}	8.6×10^{5}	192.6	(*75*)
Thin films	ZnO:Polymer – films	360	~500	1.25×10^{-3}	-9	5×10^{6}	721-1001	10^{14} - 10^{15}	$(2.5\text{-}3.4)\times10^{5}$	0.725	(*76*)
	Graphene:β-Ga_2O_3 – films	254	2	0.3	2	8×10^{7}	1.48	2.2×10^{12}	7.3×10^{2}	3.1×10^{5}	(*45*)
	SnSe – film	370	9	0.1	20	NM	5.5	6×10^{10}	1.8×10^{3}	NM	(*63*)
Commercial	Si	400-1100	NM	NM	10	8×10^{5}	0.5	3×10^{12}	NM	1×10^{-6}	(*52*)
	GaP	150-550	NM	NM	5	4.8×10^{6}	0.1	2×10^{13}	NM	1.1×10^{-4}	
	Ge	800-1800	NM	NM	3	7.1×10^{6}	0.8	3×10^{11}	NM	1.2×10^{-3}	
	InGaAs	900-1700	NM	NM	6	18×10^{3}	0.9	NM	NM	3.5×10^{-7}	

Table 1 | Comparison of key features of our work based on SnS nanosheets with previously reported state-of-the-art photodetectors. NM: Not mentioned, P_{inc}: Illumination power density, V: Voltage bias, R: Responsivity, D^*: Detectivity, EQE: External Quantum Efficiency, Ref: References

EXPERIMENTAL

***Material Synthesis and Fabrication*:** Experiments were conducted in a controlled environment in a specially designed glove box. Initially, a continuous supply of nitrogen at a flow rate 0.5 sccm was maintained for about 4 h to ensure complete removal of oxygen. After which, H_2S gas was introduced at a flow rate of 0.5 sccm for 1 h to attain a homogeneous sulfide rich atmosphere within the glove box. Elemental tin was molten with the aid of a ceramic heater at a temperature of 350°C by applying a voltage of 12 V using a power supply unit. The initial thick layer from the surface of molten metal was removed through pre-

conditioning prior to transferring freshly grown nanosheets onto desired substrates (SiO_2, Si, glass, TEM grids, *etc*). The freshly formed liquid metal undergoes a colour change from silver to dull yellow within a few seconds confirming the formation of the metal sulfide layer on the surface of metal-melt. Prior to touch printing, substrates were placed on the heater to avoid thermal shock. When TEM grids were utilized for transferring the material, the grids were placed on PDMS to avoid breakage of the fragile grids. Standard photolithography was used to pattern electrodes. Metal Cr (10 nm)/Au (100 nm) was deposited on the developed patterns using electron beam evaporation technique at a pressure less than 3×10^{-7} mbar. Lift - off was done in acetone to reveal the required metal contacts.

Structural Characterisations: Atomic force microscopy (AFM) measurement was conducted using the Bruker Dimension Icon AFM in ScanAsyst mode. Raman spectra were obtained on $SnS/SiO_2/Si$ samples using the Horiba Scientific Raman spectrometer utilizing 532 nm laser source operating at 9 mW excitation power, 50× objective, and 1800 grating. XPS was carried out using a Thermo K-Alpha instrument equipped with a monochromatic Al Kα source (photon energy of 1486.7 eV and pressure of 1×10^{9} mbar). UV-*vis* absorbance measurements were collected using a CRAIC 20/30 microspectrophotometer. The obtained binding energy was calibrated using C 1s peak at 284.8 eV.

Low magnification TEM and HRTEM were conducted using JEOL 1010 and 2100F microscopes. The JEOL 1010 was equipped with a Gatan Orius SC600A CCD camera and operated at an accelerating voltage of 100 keV. JEOL 2100F microscope was equipped with a Gatan Orius SC1000 CCD camera. This instrument has an accelerating voltage of 80 keV.

Electrical and Optoelectronic Measurements: Electrical measurements were carried out using the B2901A source meter and FET measurements were carried out using the Keithley 4200SCS semiconductor parameter analyser. For the optoelectronic measurements, commercial monochromatic light emitting diodes (Thorlabs, Inc.) with different wavelengths ranging from 280 nm to 850 nm were used as excitation sources. All measurements were performed in the dark and ambient light with exposure to only the target illumination wavelengths. The illumination power was calibrated by a commercial UV-enhanced photodetector (Newport Corporation). The laser beam was directed onto the nanosheets vertically at a fixed distance of about 1.7 cm from the sample holder. Electrical characterisations for various light sources were repeated under different illumination intensities in the range of 0.5 to 2.5 mW/cm^2.The shape of the beam of light is Gaussian in

nature. The frequency and pulse width modulation of the light sources were performed by using the Arduino-Uno programmable microcontroller board.

The photocurrent was detected using a lock-in detection system including an Agilent 33210A 10MHz function/arbitrary waveform generator, a Stanford SR570 low-noise current pre-amplifier and a Stanford SR850 digital lock-in amplifier. (The reflected light was measured simultaneously using a confocal microscope and a Si avalanche photodiode (APD) detector). The generator frequency is 333 Hz and the applied voltage is 4V.

Acknowledgments

The authors would also like to acknowledge the ARC for funding received under the ARC Discovery Project scheme (DP180102752). This work was performed in part at the RMIT Micro Nano Research Facility (MNRF) in the Victorian Node of the Australian National Fabrication Facility (ANFF). The authors also acknowledge the facilities, and the scientific and technical assistance of the RMIT Microscopy & Microanalysis Facility (RMMF), a linked laboratory of Microscopy Australia. The DFT computation was supported by the Multi-modal Australian ScienceS Imaging and Visualisation Environment (MASSIVE) (www.massive.org.au) and was undertaken with the assistance of resources and services from the National Computational Infrastructure (NCI), which is supported by the Australian Government. Additional support and work were provided by the Pawsey Supercomputing Centre with funding from the Australian Government and the Government of Western Australia.

REFERENCES

1. Z. Tian, C. Guo, M. Zhao, R. Li, J. Xue, Two-Dimensional SnS: A Phosphorene Analogue with Strong In-Plane Electronic Anisotropy. *ACS Nano* **11**, 2219-2226 (2017).
2. H. Wang, X. Qian, Two-dimensional multiferroics in monolayer group IV monochalcogenides. *2D Materials* **4**, (2017).
3. P. Z. Hanakata, A. Carvalho, D. K. Campbell, H. S. Park, Polarization and valley switching in monolayer group-IV monochalcogenides. *Journal of Physical Review B* **94**, 035304 (2016).
4. L. C. Gomes, A. Carvalho, A. C. Neto, Vacancies and oxidation of two-dimensional group-IV monochalcogenides. *Journal of Physical Reviews B* **94**, 054103 (2016).
5. Z. Hu *et al.*, Recent progress in 2D group IV–IV monochalcogenides: synthesis, properties and applications. *Nanotechnology* **30**, 252001 (2019).
6. J. R. Brent *et al.*, Tin (II) sulfide (SnS) nanosheets by liquid-phase exfoliation of herzenbergite: IV–VI main group two-dimensional atomic crystals. *Journal of the American Chemical Society* **137**, 12689-12696 (2015).
7. C. Xin *et al.*, Few-layer tin sulfide: a new black-phosphorus-analogue 2D material with a sizeable band gap, odd–even quantum confinement effect, and high carrier mobility. *The Journal of Physical Chemistry C* **120**, 22663-22669 (2016).
8. M. Patel, A. Chavda, I. Mukhopadhyay, J. Kim, A. J. N. Ray, Nanostructured SnS with inherent anisotropic optical properties for high photoactivity. *Nanoscale* **8**, 2293-2303 (2016).
9. Q. Zhang, X. Chen, W.-C. Liu, Y. Wang, Stacking effect on electronic, photocatalytic and optical properties: A comparison between bilayer and monolayer SnS. *Computational Materials Science* **158**, 272-281 (2019).
10. A. Arash *et al.*, Large-area synthesis of 2D MoO_{3-x} for enhanced optoelectronic applications. *2D Materials* **6**, 035031 (2019).
11. G. Yue *et al.*, Structure and optical properties of SnS thin film prepared by pulse electrodeposition. *Journal of Alloys and Compounds* **468**, 254-257 (2009).
12. L. Pan, S. Yuan, J. Lin, B. Zou, L.-J. Shi, The tunable bandgap effect of SnS films. *Journal of Physics: Condensed Matter* **30**, 465302 (2018).
13. Z. Deng *et al.*, Solution synthesis of ultrathin single-crystalline SnS nanoribbons for photodetectors via phase transition and surface processing. *ACS Nano* **6**, 6197-6207 (2012).
14. K. R. Reddy, N. K. Reddy, R. Miles, Photovoltaic properties of SnS based solar cells. *Solar Energy Materials and Solar Cells* **90**, 3041-3046 (2006).
15. S. Sucharitakul *et al.*, Screening limited switching performance of multilayer 2D semiconductor FETs: the case for SnS. *Nanoscale* **8**, 19050-19057 (2016).
16. L. Makinistian, E. A. Albanesi, On the band gap location and core spectra of orthorhombic IV–VI compounds SnS and SnSe. *Basic Solid State Physics* **246**, 183-191 (2009).
17. L. S. Price *et al.*, Atmospheric pressure chemical vapor deposition of tin sulfides (SnS, Sn_2S_3, and SnS_2) on glass. *Chemistry of Materials* **11**, 1792-1799 (1999).
18. P. Sinsermsuksakul, J. Heo, W. Noh, A. S. Hock, R. G. Gordon, Atomic Layer Deposition of Tin Monosulfide Thin Films. *Advanced Energy Materials* **1**, 1116-1125 (2011).
19. L. A. Burton *et al.*, Synthesis, Characterization, and Electronic Structure of Single-Crystal SnS, Sn_2S_3, and SnS_2. *Chemistry of Materials* **25**, 4908-4916 (2013).
20. N. Higashitarumizu *et al.*, Self-passivated ultra-thin SnS layers via mechanical exfoliation and post-oxidation. *Nanoscale* **10**, 22474-22483 (2018).
21. H.-Y. Song, J.-T. Lü, Density functional theory study of inter-layer coupling in bulk tin selenide. *Chemical Physics Letters* **695**, 200-204 (2018).
22. A. Zavabeti *et al.*, A liquid metal reaction environment for the room-temperature synthesis of atomically thin metal oxides. *Science* **358**, 332-335 (2017).
23. B. J. Carey *et al.*, Wafer-scale two-dimensional semiconductors from printed oxide skin of liquid metals. *Nature communications* **8**, 1-10 (2017).
24. T. Daeneke *et al.*, Wafer-scale synthesis of semiconducting SnO monolayers from interfacial oxide layers of metallic liquid tin. *ACS Nano* **11**, 10974-10983 (2017).

25. J. Xia *et al.*, Physical vapor deposition synthesis of two-dimensional orthorhombic SnS flakes with strong angle/temperature-dependent Raman responses. *Nanoscale* **8**, 2063-2070 (2016).
26. M. Li *et al.*, Revealing anisotropy and thickness dependence of Raman spectra for SnS flakes. *RSC advances* **7**, 48759-48765 (2017).
27. A. Lambros, D. Geraleas, N. Economou, Optical absorption edge in SnS. *Journal of Physics and Chemistry of Solids* **35**, 537-541 (1974).
28. A. Rauf *et al.*, Non-stoichiometric SnS microspheres with highly enhanced photoreduction efficiency for Cr (VI) ions. *RSC Advances* **7**, 30533-30541 (2017).
29. G. Matyszczak *et al.*, Application of sonochemically synthesized SnS and SnS2 in the electro-Fenton process: kinetics and enhanced decolorization. *Ultrasonics Sonochemistry*, 105186 (2020).
30. E. Guneri *et al.*, Properties of p-type SnS thin films prepared by chemical bath deposition. *Chalcogenide Letters* **7**, 685-694 (2010).
31. J. Vidal *et al.*, Band-structure, optical properties, and defect physics of the photovoltaic semiconductor SnS. *Applied Physics Letters* **100**, 032104 (2012).
32. R. S. Datta *et al.*, Two dimensional $PbMoO_4$: A photocatalytic material derived from a naturally non-layered crystal. *Nano Energy* **49**, 237-246 (2018).
33. T. Leijtens *et al.*, Carrier trapping and recombination: the role of defect physics in enhancing the open circuit voltage of metal halide perovskite solar cells. *Energy & Environmental Science* **9**, 3472-3481 (2016).
34. A. White, Generation-recombination processes and Auger suppression in small-bandgap detectors. *Journal of Crystal Growth* **86**, 840-848 (1988).
35. Y. Fang, Q. Dong, Y. Shao, Y. Yuan, J. Huang, Highly narrowband perovskite single-crystal photodetectors enabled by surface-charge recombination. *Nature Photonics* **9**, 679 (2015).
36. S. Hwan Lee *et al.*, High-performance photocurrent generation from two-dimensional WS_2 field-effect transistors. *Applied Physics Letters* **104**, 193113 (2014).
37. N. Perea-López *et al.*, CVD-grown monolayered MoS_2 as an effective photosensor operating at low-voltage. *2D Materials* **1**, 011004 (2014).
38. E. Putley, Indium antimonide submillimeter photoconductive detectors. *Applied Optics* **4**, 649-657 (1965).
39. T. Ahmed *et al.*, Multifunctional optoelectronics via harnessing defects in layered black phosphorus. *Advanced Functional Materials* **29**, 1901991 (2019).
40. S. Chen *et al.*, A Flexible UV–Vis–NIR Photodetector based on a Perovskite/Conjugated-Polymer Composite. *Advanced Materials* **28**, 5969-5974 (2016).
41. C. Xie, P. You, Z. Liu, L. Li, F. Yan, Ultrasensitive broadband phototransistors based on perovskite/organic-semiconductor vertical heterojunctions. *Light: Science & Applications* **6**, e17023-e17023 (2017).
42. L. Dou *et al.*, Solution-processed hybrid perovskite photodetectors with high detectivity. *Nature Communications* **5**, 5404 (2014).
43. C. Xie, C. K. Liu, H. L. Loi, F. Yan, Perovskite- Based Phototransistors and Hybrid Photodetectors. *Advanced Functional Materials* **30**, 1903907 (2020).
44. C. Xie, C. Mak, X. Tao, F. Yan, Photodetectors based on two- dimensional layered materials beyond graphene. *Advanced Functional Materials* **27**, 1603886 (2017).
45. W. Y. Kong *et al.*, Graphene- β- Ga_2O_3 heterojunction for highly sensitive deep UV photodetector application. *Advanced Materials* **28**, 10725-10731 (2016).
46. X. Gong *et al.*, High-detectivity polymer photodetectors with spectral response from 300 nm to 1450 nm. *Science* **325**, 1665-1667 (2009).
47. A. Gundimeda *et al.*, Fabrication of non-polar GaN based highly responsive and fast UV photodetector. *Applied Physics Letters* **110**, 103507 (2017).
48. S. K. Jain *et al.*, GaN-UV photodetector integrated with asymmetric metal semiconductor metal structure for enhanced responsivity. *Journal of Materials Science: Materials in Electronics* **29**, 8958-8963 (2018).

49. Y. Huang *et al.*, Tin Disulfide - An Emerging Layered Metal Dichalcogenide Semiconductor: Materials Properties and Device Characteristics. *ACS nano* **8**, 10743-10755 (2014).
50. R. Cheng *et al.*, Ultrathin Single- Crystalline CdTe Nanosheets Realized via Van der Waals Epitaxy. *Advanced Materials* **29**, 1703122 (2017).
51. T. Ahmed *et al.*, Optically Stimulated Artificial Synapse Based on Layered Black Phosphorus. *Small* **15**, 1900966 (2019).
52. . (Thorlabs Inc., https://www.thorlabs.com/newgrouppage9.cfm?objectgroup_id=285, 2020), vol. 2020.
53. R. Saran, R. Curry, Lead sulphide nanocrystal photodetector technologies. *Nature Photonics* **10**, 81 (2016).
54. G. Konstantatos, E. H. Sargent, Solution-processed quantum dot photodetectors. *Proceedings of the IEEE* **97**, 1666-1683 (2009).
55. P. Martyniuk, A. Rogalski, HOT infrared photodetectors. *Opto-Electronics Review* **21**, 239-257 (2013).
56. T. Yagi, Y. Fujiwara, T. Nishino, Y. Hamakawa, Photoluminescence and lattice mismatch in InGaAs/InP. *Japanese Journal of Applied Physics* **22**, L467 (1983).
57. I. Kimukin *et al.*, InGaAs-based high-performance pin photodiodes. *IEEE Photonics Technology Letters* **14**, 366-368 (2002).
58. A. R. Hong *et al.*, Core/shell-structured upconversion nanophosphor and cadmium-free quantum-dot bilayer-based near-infrared photodetectors. *Optics Letters* **40**, 4959-4962 (2015).
59. T. Ahmed *et al.*, Degradation of black phosphorus is contingent on UV–blue light exposure. *npj 2D Materials and Applications* **1**, 1-7 (2017).
60. J. D. Wood *et al.*, Effective passivation of exfoliated black phosphorus transistors against ambient degradation. *Nano Letters* **14**, 6964-6970 (2014).
61. O. Lopez-Sanchez, D. Lembke, M. Kayci, A. Radenovic, A. Kis, Ultrasensitive photodetectors based on monolayer MoS_2. *Nature Nanotechnology* **8**, 497 (2013).
62. A. Di Bartolomeo *et al.*, Electrical transport and persistent photoconductivity in monolayer MoS_2 phototransistors. *Nanotechnology* **28**, 214002 (2017).
63. J. Yao, Z. Zheng, G. Yang, All- layered 2D optoelectronics: a high- performance UV–vis–NIR broadband SnSe photodetector with Bi_2Te_3 topological insulator electrodes. *Advanced Functional Materials* **27**, 1701823 (2017).
64. X. Zhou, Q. Zhang, L. Gan, H. Li, T. Zhai, Large- size growth of ultrathin SnS_2 nanosheets and high performance for phototransistors. *Advanced Functional Materials* **26**, 4405-4413 (2016).
65. N. Koteeswara Reddy, M. Devika, E. Gopal, Review on tin (II) sulfide (SnS) material: synthesis, properties, and applications. *Critical Reviews in Solid State Material Sciences* **40**, 359-398 (2015).
66. J. Chu *et al.*, High- performance ultraviolet photodetector based on a few- layered 2D $NiPS_3$ nanosheet. *Advanced Functional Materials* **27**, 1701342 (2017).
67. P. Hu, Z. Wen, L. Wang, P. Tan, K. Xiao, Synthesis of few-layer GaSe nanosheets for high performance photodetectors. *ACS nano* **6**, 5988-5994 (2012).
68. W. Choi *et al.*, High- detectivity multilayer MoS_2 phototransistors with spectral response from ultraviolet to infrared. *Advanced Materials* **24**, 5832-5836 (2012).
69. E. Liu *et al.*, High responsivity phototransistors based on few- layer ReS_2 for weak signal detection. *Advanced Functional Materials* **26**, 1938-1944 (2016).
70. X. Zhou *et al.*, Ultrathin $SnSe_2$ Flakes Grown by Chemical Vapor Deposition for High-Performance Photodetectors. *Advanced Materials* **27**, 8035-8041 (2015).
71. Y. Xu *et al.*, Selenium- doped black phosphorus for high- responsivity 2D photodetectors. *Small* **12**, 5000-5007 (2016).
72. H. Tan *et al.*, Ultrathin 2D Photodetectors Utilizing Chemical Vapor Deposition Grown WS_2 With Graphene Electrodes. *ACS Nano* **10**, 7866-7873 (2016).
73. L. Li *et al.*, Single- crystalline CdS nanobelts for excellent field- emitters and ultrahigh quantum- efficiency photodetectors. *Advanced Materials* **22**, 3161-3165 (2010).

74. X. Zhou *et al.*, High performance near-infrared photodetectors based on ultrathin SnS nanobelts grown *via* physical vapor deposition. *Journal of Materials Chemistry C* **4**, 2111-2116 (2016).
75. D. Zheng *et al.*, High- performance ferroelectric polymer side- gated CdS nanowire ultraviolet photodetectors. *Advanced Functional Materials* **26**, 7690-7696 (2016).
76. F. Guo *et al.*, A nanocomposite ultraviolet photodetector based on interfacial trap-controlled charge injection. *Nature nanotechnology* **7**, 798-802 (2012).

Liquid-metal synthesised ultra-thin SnS layers for high-performance broadband photodetectors

Vaishnavi Krishnamurthi[1], Hareem Khan[1], Taimur Ahmed[1,2], Ali Zavabeti[1,3], Sherif Abdulkader Tawfik[4], Shubhendra Kumar Jain[1,2,5,6], Michelle J. S. Spencer[4], Sivacarendran Balendhran[7], Kenneth B Crozier[7,8,9], Ziyuan Li[10], Lan Fu[10], Md Mohiuddin[1], Mei Xian Low[1,2], Babar Shabbir[11], Andreas Boes[1], Arnan Mitchell[1], Christopher F McConville[4], Yongxiang Li[1], Kourosh Kalantar-Zadeh[12], Nasir Mahmood[1,]* and Sumeet Walia[1,2]**

[1]School of Engineering, RMIT University, 124 La Trobe Street, Melbourne, VIC, 3001, Australia

[2]Functional Materials and Microsystems Research Group and the Micro Nano Research Facility, RMIT University, 124 La Trobe Street, Melbourne, VIC 3001, Australia

[3]Department of Chemical Engineering, The University of Melbourne, VIC 3010, Australia

[4]School of Science, RMIT University, Melbourne, VIC 3001, Australia

[5]Sensor Device Metrology Group, CSIR - National Physical Laboratory (CSIR-NPL), Dr K. S. Krishnan Road, New Delhi-110012, India.

[6]Academy of Scientific & Innovative Research, (AcSIR), CSIR-HRDC Campus, Ghaziabad, Uttar Pradesh 201002, India.

[7]School of Physics, The University of Melbourne, 3010, Australia.

[8]Department of Electrical and Electronic Engineering, The University of Melbourne, VIC 3010, Australia

[9]Australian Research Council (ARC) Centre of Excellence for Transformative Meta-Optical Systems, The University of Melbourne, VIC 3010, Australia

[10]Australian Research Council (ARC) Centre of Excellence for Transformative Meta-Optical Systems, The Australian National University, Canberra, ACT 3001, Australia

[11]Department of Materials Science and Engineering, Monash University, Clayton, Victoria, 3800, Australia

[12]School of Chemical Engineering, University of New South Wales (UNSW), Sydney, NSW 2052, Australia

*Correspondence:
nasir.mahmood@rmit.edu.au, taimur.ahmed@rmit.edu.au, sumeet.walia@rmit.edu.au

Miniaturised photodetectors are key for the next generation of sensing, communication and imaging technologies. Single-atom thick SnS layers are printed on a millimetre scale to showcase application in high-performance photodetectors. These SnS based ultra-fast photodetectors show a broadband spectral response ranging from deep ultraviolet (UV) to near infrared (NIR) wavelengths (*i.e.*, 280 nm to 850 nm) with excellent figures of merit.